Novel Charge-Ordered States in 1*T*-$IrTe_2$

Jinwoong Hwang[1*] and Sung-Kwan Mo[2*]

[1]*Department of Physics and Institute of Quantum Convergence Technology, Kangwon National University, Chuncheon, Korea.*

[2]*Advanced Light Source, Lawrence Berkeley National Laboratory, Berkeley, CA, USA.*

Abstract

1*T*-$IrTe_2$ exhibits an intriguing series of charge-ordered states in both bulk and atomically thin layers. The charge orders in $IrTe_2$ emerge with consecutive first-order structural transitions involving in-plane Ir-Ir dimerization and interlayer Te-Te depolymerization, resulting in stripe patterns with various periods. Upon chemical doping, 1*T*-$IrTe_2$ can also be driven into a superconductor. Despite the intense research effort, a comprehensive understanding of the nature of the charge ordering and its relation to the superconductivity is yet to be reached. This review provides an overview of the novel charge orders and the emergence of superconductivity in $IrTe_2$. We further introduce the recent studies on $IrTe_2$ nanoflake, in which novel charge orders attainable only in two-dimensional limits lay the grounds for an exotic phase diagram.

* Corresponding authors: jwhwang@kangwon.ac.kr, skmo@lbl.gov

Section 1: Introduction

The investigation of the ordered phases that spontaneously lower the symmetry of condensed matter systems is fundamental to understanding the physical properties of quantum materials [1]. Charge order is one of the most ubiquitous such ordered phases that manifests itself as a spontaneous reorganization of electrons, which arises from the complex interplay of electron-electron interactions, lattice distortions, and crystal fields [2-4]. In many complex quantum materials, charge orders occur near other ordered states with similar energy scales, indicating a small variance in the interplay among spin, charge, lattice, and orbital degrees of freedom may drive the materials system into completely different ground states [4-9]. For example, in unconventional superconductors, charge orders are typically found adjacent to the superconducting dome in the phase diagram, although whether these two ordered states compete or coexist is a subject of ongoing debate [3,5,9]. More recently, the boom of research on two-dimensional (2D) materials uncovers novel charge orders, suggesting that the reduced dimensionality is one of the key factors influencing the charge orders due to the changes in symmetry, limited phase space, and enhanced electron-electron interactions [10-12]. An improved understanding of charge ordering phenomena in relation to their concurrent ordered phases would provide us with a deeper understanding of the emergent properties in quantum materials and direct us toward engineering materials with tailored properties for innovative technological applications.

Iridium ditelluride in the 1*T* structural phase (1*T*-$IrTe_2$) is a fascinating compound in this regard. It belongs to a class of materials known as transition metal dichalcogenides (TMDC), which has a triangular lattice of Ir ions by edge-sharing $IrTe_6$ octahedra in the layered structures, as shown in Fig. 1(a). Compared to the conventional van der Waals (vdW) layered materials, a standout property of 1*T*-$IrTe_2$ is that its ratio between in-plane (a = 3.93 Å) and out-of-plane lattice constants (c = 5.39 Å), c/a = 1.37, is much smaller than

c/a = 1.6 ~ 1.8 in other isostructural TMDC materials [13-15]. The Te-Te interlayer distance (3.50 Å) is also much shorter than the expected vdW bond length $2R_{vdW}$ = 4.12 Å, indicating strong interlayer coupling that makes $(Te_2)^{3-}$ polymeric bonds and Ir^{3+} valence configuration [15]. In addition, the combined effects of strong spin-orbit coupling of Ir and a three-dimensional band structure due to the strong Te-Te interlayer coupling induce type-II Dirac dispersions protected by C_{3v} symmetry [16,17]. Upon cooling, 1*T*-$IrTe_2$ undergoes a structural phase transition from trigonal ($P\bar{3}m1$) to triclinic ($P\bar{1}$) structures accompanied by anomalies in electrical resistivity and magnetic susceptibility [15,18]. More importantly, it goes through a cascade of charge ordering with decreasing temperatures [15,19-22]. The charge-ordering transition in 1*T*-$IrTe_2$ looks distinct from a conventional charge density wave (CDW): first-order transition to a commensurate structure results in a heavy reconstruction of electronic structure over a large energy window [23-27]. The phonon softening signifying the structural instability was not found in the phonon dispersion of the bulk 1*T*-$IrTe_2$ [28]. Furthermore, unlike most TMDCs with superconducting ground state, for which the pressure suppresses the CDW but enhances the superconductivity, the opposite trend was observed in 1*T*-$IrTe_2$ [29,30]. Due to these exotic properties, 1*T*-$IrTe_2$ is a fascinating materials platform to study the relationship between structural phase transitions, charge orderings, band topology, and superconductivity.

In this review, we mainly focus on charge-ordered phases in bulk and atomically thin 1*T*-$IrTe_2$. **Section 2** presents the charge orders in bulk and surface of $IrTe_2$. **Section 3** elaborates on the relations between the charge ordering and the superconductivity for cation- and anion-substituted, and thickness-controlled 1*T*-$IrTe_2$. **Section 4** introduces the novel charge order realized in monolayer (ML) 1*T*-$IrTe_2$. A final summary and outlook are presented in **Section 5**.

Section 2: Stripe charge orders in bulk and surface of 1*T*-$IrTe_2$

Bulk 1*T*-$IrTe_2$ stabilizes with a shorter interlayer distance than the expected vdW bond length, which implies a stronger Te-Te interlayer coupling [13-15]. The charge orders in bulk and surface 1*T*-$IrTe_2$ show different behaviors. In bulk, 1*T*-$IrTe_2$ exhibits two consecutive first-order transitions at 280 K and 180 K, accompanied by anomalies in electrical resistivity and magnetic susceptibility [18-22], as shown in Figs. 1(b,c). Concomitantly, superstructural modulations have been observed from $1 \times 1 \times 1$ (trigonal 1*T* structure) at high temperatures (HT) to $5 \times 1 \times 5$ at ~280 K and $8 \times 1 \times 8$ at ~180 K, respectively. The superstructures were characterized by transmission electron microscopy (TEM) [29] and X-ray diffraction (XRD) studies [18,31-33], and the ordering wave vectors $\mathbf{q}_{1/5}$ = (1/5 0 1/5) and $\mathbf{q}_{1/8}$ = (1/8 0 1/8) have been verified, respectively. Upon cooling from the HT to $\mathbf{q}_{1/5}$ transition temperature, in-plane lattice constant *a* decreases, while out-of-plane lattice constant *c* increases, resulting in an increase of the *c*/*a* ratio from 1.37 (HT phase) to 1.40 ($\mathbf{q}_{1/5}$ phase) [15]. The ratio further increases to 1.42 across the $\mathbf{q}_{1/5}$ to $\mathbf{q}_{1/8}$ transition. In contrast, on heating, the $\mathbf{q}_{1/8}$ phase directly transits into the HT phase at 280 K (Fig. 2), and the *c*/*a* ratio is reduced back to 1.37 in the HT phase. The stripe charge-ordered phases of 1*T*-$IrTe_2$ stay metallic because Ir-Ir dimerization and Te-Te depolymerization at LT produce conducting planes running across the vdW gaps in between the dimer planes [15,20,32-35].

The increased *c*/*a* ratios in the $\mathbf{q}_{1/5}$ and $\mathbf{q}_{1/8}$ phases imply certain degrees of the $(Te_2)^{3-}$ interlayer bond breaking, which leads to partial Ir valence change from Ir^{3+} (d^6) at HT to Ir^{4+} (d^5) at low temperature (LT) [15,21,35] as shown in Fig. 1(e). As a result, Ir^{3+}-Ir^{4+} charge-ordered phases form with periodic lattice distortions (Fig. 1(d)). Moreover, Ir-Ir bond length decreases with in-plane Ir^{4+}-Ir^{4+} dimerization in LT phases by up to 20%, which can be

clearly observed as large shifts in the Ir 4*f* core levels (Fig. 1(e)) [15,19,21]. Such a significant contraction of the lattice in $IrTe_2$ cannot be understood within conventional CDW pictures [23-27,32-40]. Strong spin-orbit coupling is another important aspect to consider for a comprehensive understanding of Ir compounds [41-43]. Diamagnetic spin-orbit Mott dimer states due to a strong spin-orbit coupling of Ir atoms were also suggested for LT phases of 1*T*-$IrTe_2$ under a mean-field description [15,27].

At the surface of 1*T*-$IrTe_2$, the charge-ordered phases are quite different and more complex compared to the bulk case due to the different coupling along the *c*-axis direction [44-47]. Scanning tunneling microscopy (STM) studies found additional 11×1 and 17×1 surface modulations at LT (Fig. 2), with the tendency to generate a (3*n*+2) structure, where *n* is an integer indicating the number of dimers in a unit cell [44-46]. More interestingly, a 6×1 superstructure, not seen in bulk, is observed as the ground state of the charge ordering at the LT surface. The surface transition temperatures are quite different from those of the bulk (Fig. 2), with several periodicities coexisting, which resembles the devil's staircase behavior [46,47]. A key feature observed in the 6×1 charge order at the surface of 1*T*-$IrTe_2$ is more complete Ir dimer formations compared to the bulk (Fig. 1(d) and Fig. 2). The tendency to create more Ir dimers on the surface demonstrates the significance of Te-Te interlayer coupling and its breaking in the formation of the charger orders in 1*T*-$IrTe_2$ [45-51], considering the ordering involves Ir 5*d* to Te 5*p* charge transfer with Te polymeric bond breaking and the surface has a weaker interlayer coupling due to the absence of the upper layer [15,29,35].

To understand the distinct charge ordering in 1*T*-$IrTe_2$, various mechanisms have been proposed. Since the hump structures of electrical resistivity and the step-like reduction of the magnetic susceptibility (Figs. 1(b,c)) with the structural phase transition are often

observed in the CDW materials, a Peierls-type CDW scenario was first suggested as the origin of the structural phase transition in 1*T*-$IrTe_2$ [18]. However, the gap opening expected for the CDW transition was not observed in nuclear magnetic resonance (NMR) spectra [52], optical conductivity [34,38,53] and angle-resolved photoemission spectroscopy (ARPES) [23-27]. In addition, the CDW picture based on the Fermi surface nesting only provides the charge ordering vector $\mathbf{q}_{1/5}$ and cannot describe the charge ordering with $\mathbf{q}_{1/8}$ in bulk and $\mathbf{q}_{1/6}$ at the surface. A number of different mechanisms, including the orbital-induced Peierls instability [24,25], local bonding instabilities of Te 5*p* orbitals [28,54,55], the van Hove singularity at the Fermi level [21], subtle balance in local interactions of Ir-Ir dimerization and Te-Te depolymerization [15,29,35], and an order-disorder transition [39], have been proposed to explain the origin of the charge ordering. The exact nature and the driving force of the charge-ordered phases in 1*T*-$IrTe_2$ are still the subject of further investigation.

Section 3: Tuning the charge-ordered phases in the vicinity of superconductivity

Charge orders are often found in the vicinity of other quantum orders, such as magnetism and superconductivity [3-5,9]. While it is difficult to nail down whether the charge order competes or cooperates with other ordered phases, tuning the material properties around the charge-ordered phases by doping, gating, strain, thickness control, and other stimuli offers an ample opportunity to engineer novel functionalities and to explore new regimes of quantum phenomena [3,9]. In this section, we review works related to tuning charge orders and their interplay with superconductivity in 1*T*-$IrTe_2$ by chemical doping and thickness control.

3.1 The emergence of the superconductivity in $Ir_{1-x}M_xTe_2$

Superconductivity in the vicinity of a competing electronic order often manifests itself with a superconducting dome, centered around a presumed quantum critical point in the phase diagram [3,5,9]. This common feature, found in many unconventional superconductors and TMDC superconductors, has supported a prevalent scenario in which fluctuations or partial melting of a parent order are essential for inducing or enhancing superconductivity [3-5,9]. A dome-shaped superconducting phase diagram appears in 1*T*-$IrTe_2$ by chemical doping (Fig. 3), similar to many TMDCs hosting CDW orders in the parent compounds [18,54-65].

As shown in Fig. 3, superconductivity in $IrTe_2$ emerges when the charge orders are suppressed by Pt, Pd (electron doping) [18,57-64] or Rh (isovalent doping) substitution [55,56] for Ir, or intercalation of Cu and Pd [18,54,64]. The superconducting transition temperature (T_c) of $Ir_{1-x}Pt_xTe_2$ reaches a maximum of ~3.1 K for $x = 0.04$ [57]. With an increased level of substitution, the in-plane (out-of-plane) lattice parameters of $Ir_{1-x}Pt_xTe_2$ and $Ir_{1-x}Pd_xTe_2$ increase (decrease) monotonically [18,57,59,66], while that of $Ir_{1-x}Rh_xTe_2$ does not change [55]. Since $RhTe_2$ can be partially crystallized in polymeric CdI_2 structure, with lattice parameters and an octahedral distortion similar to those in $IrTe_2$, partial substitution of Ir by Rh leads to little change of lattice parameters [55]. Despite the close similarity of the structures, the electron transfer between Te and transition metals would be much different from Rh and Ir cases, since Ir has more extended 5*d* orbitals [55,56,67]. This covalency difference leads to a modification in the dimerization with increased Rh doping and consequently alters the nature of the charge order and the onset of the emergence of superconductivity [64,67,68]. As a result, the doping level of Rh required to suppress the charge order and induce superconductivity is three times larger than that of Pt (Fig. 3). These results suggest that the suppression of the charge order and the emergence of

superconductivity are related to the changes of lattice parameters and the covalency in 1*T*-$IrTe_2$ [64-68].

On the other hand, the anion-substitution or the application of hydrostatic pressure in 1*T*-$IrTe_2$ just increases the charge ordering temperature without entering the superconducting phase (Fig. 3) [29,30,64,68-71]. This behavior contrasts with many previously studied CDW materials in the proximity of superconductivity; in many cases, both pressure and the anion-substitution suppress the charge order and induce the superconducting dome in their phase diagrams [3-5]. The Se substitution of Te and hydrostatic pressure drastically increases the charge ordering temperature of $IrTe_2$ from 280 K to 560 K with a sudden increase of *c*/*a* ratio [29]. Concomitantly, this enhancement is accompanied by the evolution of non-sinusoidal structure modulations from $\mathbf{q}_{1/5}$ to $\mathbf{q}_{1/6}$ charge-ordered phases [29,64,68]. The increase in the *c*/*a* ratio is ensued by the weaker Te-Te interlayer coupling and the changes of effective valences to $Ir^{(3+\delta)+}$ and $(Te_2)^{(3+\delta)-}$, respectively, even at HT due to the more electronegative Se [29]. The increased portions of Ir^{4+} valence states in 1*T*-$IrTe_2$ lead to the formation of more Ir dimers in the charge-ordered phase, resulting in $6 \times 1 \times 6$ superstructure even in the bulk [29,30,64,68-71]. This result is consistent with the emergence of 6×1 superstructure at the surface $IrTe_2$ due to the weakened interlayer coupling.

3.2 Thickness and cooling rate dependent superconductivity in 1T-$IrTe_2$

Thickness control can tune the stripe charge orders and introduce superconductivity in 1*T*-$IrTe_2$ without introducing quenched disorders. As the flake thickness decreases (Fig. 4(a)), the charge ordering temperatures monotonically decrease [72,73]. This may originate from the out-of-plane elongation resulting from the thinning down process [72-76] or the substrate-induced in-plane tensile strain on the 1*T*-$IrTe_2$ nanoflakes [72], which effectively

acts as a negative pressure effect. Simultaneously, the superconductivity emerges in 1*T*-$IrTe_2$ nanoflakes at a thickness of ~ 110 nm and disappears at ~20 nm with a dome shape in the thickness-dependent phase diagram (Fig. 4(a)) [72]. The maximum T_c reaches around 3 K at ~70 nm thickness (Fig. 4(b)) [73], which is similar to the maximum value of the doped-$IrTe_2$ [18].

The thickness-dependent phase diagram significantly differs from the doping-dependent phase diagram of bulk 1*T*-$IrTe_2$. In the bulk case, the stripe charge-ordered and superconducting phases are mutually exclusive, and the coexisting region appears in the very narrow doping range [18,57-64,72]. Even in the coexisting phase, phase-separated patch structures have been observed [62,77]. However, in 1*T*-$IrTe_2$ nanoflakes, the stripe charge-ordered phase completely covers the whole regions of the sample (Fig. 4(a)), confirmed by the spatial mapping of Raman and STM measurements [72]. The characteristics of superconductivity are also distinct in nanoflakes compared to those of the doped $IrTe_2$. The superconducting gap ratio of $IrTe_2$ nanoflakes is $2\Delta_{SC}/k_BTc \sim 5.3$ [72], which is much larger than the BCS value of 3.53, and the one for the doped bulk $IrTe_2$ has $2\Delta_{SC}/k_BTc \sim 3.7$ [61]. The coexisting stripe charge order in 1*T*-$IrTe_2$ nanoflakes increases the out-of-plane coherence length and the coupling strength of superconductivity [20,72,73]. These results show a distinct feature compared to the doped bulk 1*T*-$IrTe_2$, where the cation-substitution in 1*T*-$IrTe_2$ mainly provides a source of chemical strain, which cause the reduction of Ir dimer density in charge-ordered phase and Te depolymerization, and results in the superconducting ground state more favorable [18,55,45]. On the other hand, the stripe charge ordered phase in nanoflakes 1*T*-$IrTe_2$ dominantly prevails in the macroscopic length scale and serves as a normal state for the superconductivity without its complete or partial melting [72].

A control of the cooling rate can also induce superconductivity in 1*T*-$IrTe_2$ flakes. For the standard cooling rate of 1 K / min, the stripe charge orders show up and the superconducting state is absence in $IrTe_2$ [15,76] as described in Section 2. A high cooling rate of ~10^5 K s^{-1} by using the electric-pulse heating induces a resistivity drop in $IrTe_2$ flake with T_c^{onset} ~ 3.1 K even though a zero resistance is not obtained [78]. When the more rapid thermal quenching (~10^7 K s^{-1}) is applied, the charge order states in $IrTe_2$ are fully suppressed and the thermally quenched state reaches zero resistance with T_c^{onset} ~ 3.4 K [78]. The current pulse-based rapid cooling kinetically hinders a first-order phase transition to a charge order state and induces the hidden metastable superconductivity in hexagonal $IrTe_2$ [78]. This result is consistent with the emergence of the hexagonal superconducting patches at the surface $IrTe_2$, which are locally formed and falls into a superconducting state below 3 K for the rapid cooling [77].

Section 4: Novel insulating 2 x 1 fully dimerized structure in ML 1*T*-$IrTe_2$

The absence of interlayer coupling and subsequent changes in the electronic structure and symmetry in monolayer (ML) TMDC often lead to novel physical, chemical, and optical properties distinct from the bulk [5,12]. Considering the polymeric Te-Te interlayer coupling plays a key role in the charge ordering of 1*T*-$IrTe_2$, an intriguing question is what happens in ML $IrTe_2$ where the Te-Te coupling is totally absent. Indeed, the weakened Te-Te interlayer coupling by Se-substitution, hydrostatic pressure, and at the surface of $IrTe_2$ not only stabilizes the charge order strongly with increased transition temperature but also induces the $\mathbf{q}_{1/6}$ charge order not obtainable in bulk [19,29,44,51]. These suggest a possible dramatic change in the structural and electronic properties of ML 1*T*-$IrTe_2$ due to the complete absence of the Te-Te interlayer coupling.

In order to realize ML 1*T*-$IrTe_2$, molecular beam epitaxy (MBE) was applied on bilayer graphene (BLG) substrate [79]. The MBE is a well-known strategy to synthesize high-quality atomically thin film TMDC materials [12]. The BLG substrate, in many cases for TMDC overlayers, minimizes the substrate effect due to the vdW bond and its inertness [80-85]. MBE-grown ML 1*T*-$IrTe_2$ on BLG substrate has an in-plane lattice constant of 3.90 Å, which is quite comparable to the bulk value (3.93 Å), indicating a quasi-freestanding ML film [79]. The key finding in the charge-ordered phase of ML 1*T*-$IrTe_2$ is that it only exhibits a 2×1 dimerized structure (a complete dimerization of Ir atoms), as shown in Figs. 5(a,b). This has never been obtained in bulk or surface $IrTe_2$ compounds. More surprisingly, the 2×1 dimer ground state shows an insulating state with the size of the gap larger than 1 eV (Figs. 5(c,e)), without any transition in the Ir valency nor in the size of the gap from 10 K to 300 K (Fig. 5(f)). This is remarkable because every charge-ordered phase found in $IrTe_2$, including $\mathbf{q}_{1/5}$, $\mathbf{q}_{1/8}$, and $\mathbf{q}_{1/6}$ phases, shows a metallic nature [15,27,77].

First-principle calculations find that the existence of both charge and phonon instabilities at the M point in ML 1*T*-$IrTe_2$, suggesting that 2×1 dimer structure in ML may be driven by the Fermi surface nesting induced CDW transition [79]. The Fermi surface, in particular, dominantly consists of Te 5*p* orbital, and this indicates that the role of Te atom seems important for the 2×1 dimer transition in ML 1*T*-$IrTe_2$. However, the experimentally obtained results for ML 1*T*-$IrTe_2$ are strongly deviated from the conventional CDW features. While typical CDW formation induces 1~7% lattice contraction, ML 1*T*-$IrTe_2$ shows 20% lattice contraction with a heavy electronic reconstruction, and the size of the band gap is much larger than that originated from the CDW [79]. This suggests other essential ingredients, such as the local Ir bond formation, should be added for a fuller explanation. Generally, partially filled Ir compounds prefer locally forming a direct Ir-Ir singlet due to their extended 5*d* orbital nature [86-88]. ML

$IrTe_2$ has an edge-sharing octahedral structure and only Ir^{4+} valence state (Fig. 5f) with one hole in t_{2g} states, owing to the full absence of the polymeric Te-Te interlayer coupling. Although it is difficult to discern whether nesting or local Ir bond formation is more dominant or which one triggers the other in the 2×1 dimer formation, once any perturbations are triggered, the effect of both mechanisms amplifies each other, enabling the heavy electronic reconstruction with the large band gap and huge lattice distortion [79].

The insulating 2×1 dimer structure in ML completely disappears in bilayer (BL) 1*T*-$IrTe_2$. BL 1*T*-$IrTe_2$ shows the mixed metallic superstructure of 6×1, 5×1 and 3×1 phases (Fig. 1(d)) [79], similar to the surface and Se-substituted 1*T*-$IrTe_2$ (Figs. 5(d,e)) [15,19,29,51,70]. This is because the recovered Te-Te interlayer coupling in BL suppresses the Fermi surface nesting due to the split of the Fermi surface, which in turn eliminates the phonon softening and lattice instability [79]. At the same time, Ir^{3+} state partially exists in BL, just like surface of 1*T*-$IrTe_2$, due to the additional polymeric Te-Te interlayer, and it prevents the formation of a fully dimerized structure. The suppression of the CDW instability and mixed Ir^{3+}/Ir^{4+} valence states in BL prevent the conditions for the fully dimerized 2×1 structure. Instead, 6×1 and 5×1 phases are found as the ground states, similar to the surface and Se-substituted 1*T*-$IrTe_2$ [15,29]. This novel metal-to-insulator transition from BL to ML 1*T*-$IrTe_2$ reveals that the polymeric Te-Te interlayer coupling dramatically affects the phonon and charge instabilities in $IrTe_2$, thus playing a vital role in defining the charge-ordered ground states of 1*T*-$IrTe_2$ [12,79,89]. The breakdowns of the insulating 2×1 dimer structure were also obtained by the substrate-induced strain and band hybridization [90,91]. In these cases, ML films show 3×1 and 5×1 stripe charge ordering as found in BL and the surface of $IrTe_2$.

Section 5: Summary and outlook

In summary, we first reviewed the charge-ordered states in 1*T*-$IrTe_2$ and its tunability. Bulk 1*T*-$IrTe_2$ exhibits consecutive first-order structural transitions, accompanied by anomalies in electrical resistivity, magnetic susceptibility, and the ratio of *c*/*a* lattice constants [15]. By controlling the strength of the polymeric Te-Te interlayer coupling via Se-substitution, hydrostatic pressure, and the formation of a well-ordered surface, the charge-ordered phases can be tuned to be quite different and more complex compared to the bulk [29,51,54]. The reduced strength of the interlayer coupling induces the tendency to create more Ir dimers in charge-ordered states and enhance the transition temperatures. These characteristic behaviors in 1*T*-$IrTe_2$ demonstrate that the charge order involves both interlayer Te-Te depolymerization and in-plane Ir-Ir dimerization [15,29,35].

We also reviewed how the charge orders interplay with superconductivity in 1*T*-$IrTe_2$ in response to chemical doping, cooling-rate and thickness controls. Upon chemical doping, the stripe charge-ordered state is suppressed and 1*T*-$IrTe_2$ can be transformed into a superconductor with a dome-shaped superconducting zone in the phase diagram (Fig. 3) [55-57]. The chemical doping from a cation-substitution not only serves as a source of chemical strain, but also results in the superconducting ground state by fully suppressing the charge orders in 1*T*-$IrTe_2$. The direct comparison between electron (Pt, Pd) and isovalent (Rh) doping via cation-substitutions qualitatively shows that the suppression of the charge order and the emergence of superconductivity are related to the changes of the lattice parameters and the covalency in 1*T*-$IrTe_2$. A control of the cooling rate is another way to induce superconductivity in 1*T*-$IrTe_2$. The rapid thermal quenching by electric-pulse heating fully suppresses the charge order states in $IrTe_2$ and induces the hidden metastable superconductivity in hexagonal $IrTe_2$ [78]. These results indicate that the existence of the hexagonal patches in $IrTe_2$ at LT is closely related to the emergence of superconductivity.

Thickness control can also manipulate the stripe charge orders and trigger the superconductivity in 1*T*-$IrTe_2$. Superconductivity emerges in 1*T*-$IrTe_2$ nanoflakes at a thickness of ~ 110 nm and disappears at ~20 nm, forming a superconducting dome in the thickness-dependent phase diagram [72,73]. Distinct from the chemical doping-induced superconductivity, the stripe charge-ordered phase completely covers the whole regions of the 1*T*-$IrTe_2$ nanoflakes, indicating that the stripe charge-ordered phase can be a normal state for the superconductivity, in contrast to the doped bulk 1*T*-$IrTe_2$ [72].

When thinned down to the ML limit, 1*T*-$IrTe_2$ has a new type of charge-ordered phase. ML 1*T*-$IrTe_2$ exhibits a unique insulating 2×1 dimer structure with a band gap greater than 1 eV. The complete absence of the polymeric Te-Te interlayer coupling in ML makes the Ir^{4+} valence state in all Ir atoms and a nesting condition at the Fermi surface. Peierls-like Fermi surface instability and Ir local bond formation cooperatively enhance and stabilize the fully dimerized charge order state in ML 1*T*-$IrTe_2$. In the case of BL, the recovered polymeric Te-Te interlayer coupling suppresses those conditions owing to the split of the Fermi surface and the partial existence of the Ir^{3+} valence state, hindering the fully dimerized 2×1 charge-ordered phase [79].

1*T*-$IrTe_2$ presents a fascinating complex system where the interplay among charge, orbital, spin, and lattice degrees of freedom lies at the core of the charge ordering phenomena and its adjacent quantum phases. Understanding the mechanisms behind the charge orders in 1*T*-$IrTe_2$ holds great promise for advancing our knowledge of quantum materials and correlated electron systems [3-5]. In particular, investigating how external factors such as temperature, pressure, chemical doping, and thickness control influence the charge order in 1*T*-$IrTe_2$ and related electronic and magnetic phases could offer insights into controlling and manipulating the electronic properties of quantum materials. Such tunability

also promises a future development of materials for advanced electronic, spintronic, and quantum devices.

Acknowledgment

The work at the Advanced Light Source is supported by the Department of Energy, Office of Basic Energy Sciences, under Contract No. DE-AC02-05CH11231. J.H. acknowledges support from the National Research Foundation of Korea (NRF) Grant (RS2023-00280346) and GRDC (Global Research Development Center) Cooperative Hub Program through the NRF funded by the Ministry of Science and ICT (MSIT) (RS2023-00258359).

Author contributions

J.H. and S.-K.M. initiated the project and wrote the manuscript.

Competing interests

The authors declare no competing interests.

References

(1) P. W. Anderson, *Basic notions of condensed matter physics, Frontiers in physics,* **55** (Benjamin Cummings, London, 1984)

(2) J. van den Brink and D. I. Khomskii, *J. Phys.: Condens. Matter* **20**, *434217* (2008)

(3) A. Frano, S. Blanco-Canosa, B. Keimer and J. Birgeneau, *J. Phys.: Condens. Matter* **32**, 374005 (2020)

(3) R. Comin and A. Damascelli, *Annu. Rev. Condens. Matter Phys.* **7**, 369-405 (2016)

(4) B. Keimer and J. E. Moore, *Nat. Phys* **13**, 1045-1055 (2017)

(5) J. A. Sobota, Y. He and Z.-X. Shen, *Rev. Mod. Phys.* **93**, 025006 (2021)

(6) Y. Tokura, M. Kawasaki and N. Nagaosa, *Nat. Phys*. **13**, 1056-1068 (2017)

(7) D. N. Basov, R. D. Averitt and D. Hsieh, *Nat. Mater.* **16**, 1077-1088 (2017)

(8) H. Y. Hwang, Y. Iwasa, M. Kawasaki, B. Keimer, N. Nagaosa and Y. Tokura, *Nat. Mater.* **11**, 103-113 (2012)

(9) B. Keimer, S. A. Kivelson, M. R. Norman, S. Uchida and J. Zaanen, *Nature* **518**, 179-186 (2015)

(10) A. K. Geim and I. V. Grigorieva, *Nature* **499**, 419-425 (2013)

(11) W. Li, X. Qian and J. Li, *Nat. Rev. Mater.* **6**, 829-846 (2021)

(12) J. Hwang, W. Ruan, Y. Chen, S. Tang, M. Crommie, Z.-X. Shen and S.-K. Mo, *Rep. Prog. Phys.* **87**, 044502 (2024)

(13) S. Jobic, P. Deniard, R. Brec and J. Rouxel, *Z. anorg. allg. Chem.* **598/599**, 199-215 (1991)

(14) S. Jobic, R. Brec and J. Rouxel, *J. Solid State Chem.* **96**, 169-180 (1992)

(15) K.-T. Ko, H.-H. Lee, D.-H. Kim, J.-J. Yang, S.-W. Cheong, M.J. Eom, J.S. Kim, R. Gammag, K.-S. Kim, H.-S. Kim, T.-H. Kim, H.-W. Yeom, T.-Y. Koo, H.-D. Kim and J.-H. Park, *Nat. Commun.* **6**, 7342 (2015).

(16) F. Fei, X. Bo, P. Wang, J. Ying, J. Li, K. Chen, Q. Dai, B. Chen, Z. Sun, M. Zhang, F. Qu, Y. Zhang, Q. Wang, X. Wang, L. Cao, H. Bu, F. Song, X. Wan and B. Wang, *Adv. Mater.* **30**, 1801556 (2018).

(17) J. Jiang, S. Lee, F. Fei, F. Song, E. Vescovo, K. Kaznatcheev, F. J. Walker, C. H. Ahn,

APL Mater. **8**, 061106 (2020).

(18) J. J. Yang, Y. J. Choi, Y. S. Oh, A. Hogan, Y. Horibe, K. Kim, B. I. Min and S.-W. Cheong, *Phys. Rev. Lett.* **108**, 116402 (2012)

(19) M. Rumo, C. W. Nicholson, A. Pulkkinen, B. Hildebrand, G. Kremer, B. Salzmann, M.-L. Mottas, K. Y. Ma, E. L. Wong, M. K. L. Man, K. M. Dani, B. Barbiellini, M. Muntwiler, T. Jaouen, F. O. von Rohr and C. Monney, *Phy. Rev. B* **101**, 235120 (2020)

(20) M. J. Eom, K. Kim, Y.J. Jo, J. J. Yang, E. S. Choi, B. I. Min, J.-H. Park, S.-W. Cheong and J. S. Kim, *Phys. Rev. Lett.* **113**, 266406 (2014).

(21) T. Qian, H. Miao, Z. J. Wang, X. Shi, Y. B. Huang, P. Zhang, N. Xu, L. K. Zeng, J. Z. Ma, P. Richard, M. Shi, G. Xu, X. Dai, Z. Fang, A. F. Fang, N. L. Wang and H. Ding, *New J. Phys.* **16**, 123038 (2014)

(22) L. Zhang, X. Zhu, L. Ling, C. Zhang, L. Pi and Y. Zhang, *Philosophical Magazine* **94**, 439-446 (2014)

(23) D. Ootsuki, S. Pyon, K. Kudo, M. Nohara, M. Horio, T. Yoshida, A. Fujimori, M. Arita, H. Anzai, H. Namatame, M. Taniguchi, N. L. Saini and T. Mizokawa, *J. Phys.: Conference Series* **428**, 012018 (2013)

(24) D. Ootsuki, S, Pyon, K. Kudo, M. Nohara, M. Horio, T. Yoshida, A. Fujimori, M. Arita, H. Anzai, H. Namatame, M. Taniguchi, N. L. Saini and T. Mizokawa, *J. Phys. Soc. Jpn* **82**, 093704 (2013).

(25) D. Ootsuki, Y. Wakisaka, S. Pyon, K. Kudo, M. Nohara, M. Arita, H. Anzai, H. Namatame, M. Yaniguchi, N. L. Saini and T. Mizokawa, *Phy. Rev. B.* **86**, 014519 (2021)

(26) D. Ootsuki, S. Pyon, K. Kudo, M. Nohara, M. Horio, T. Yoshida, A. Fujimori, M. Arita, H. Anzai, H. Namatame, M. Taniguchi, N. L. Saini and T. Mizokawa, *JPS Conf. Proc.* **3**, 016015 (2014)

(27) H. Lee, K.-T. Ko, K. Kim, B.-G. Park, J. Yang, S.-W. Cheong and J.-H. Park, *EPL* **120**, 47003 (2017).

(28) H. Cao, B. C. Chakoumakos, X. Chen, J. Yan, M. A McGuire, H. Yang, R. Custelcean, H. Zhou, D. J. Singh and D. Mandrus, *Phys. Rev. B* **88**, 115122 (2013)

(29) Y. S. Oh, J. J. Yang, Y. Horibe and S.-W. Cheong, *Phys. Rev. Lett.* **110**, 127209 (2013)

(30) C. W. Nicholson, M. Rumo, A. Pulkkinen, G. Kremer, B. Salzmann, M.-L. Mottas, B. Hildebrand, T. Jaouen, T. K. Kim, S. Mukherjee, K. Ma, M. Muntwiler, F. Q. von Rohr, C. Cacho, C. Monney, *Commun. Mater.* **2**, 25 (2021)

(31) T. Toriyama, M. Kobori, T. Konishi, Y. Ohta, K. Sugimoto, J. Kim, A. Fujiwara, S. Pyon, K. Kudo and M. Nohara, *J. Phys. Soc. Jpn.* **83**, 033701 (2014)

(32) G. L. Pascut, K. Haule, M. J. Gutmann, S. A. Barnett, A. Bambardi, S. Artyukhin, T. Birol, D. Vanderbilt, J. J. Yang, S.-W. Cheong and V. Kiryukin, *Phys. Rev. Lett*. **112**, 086402 (2014)

(33) G. L. Pascut, T. Birol, M. J. Gutmann, J. J. Yang, S.-W. Cheong, K. Haule and V. Kiryukhin, *Phys. Rev. B* **90**, 195122 (2014)

(34) K. Kim, S. Kim and B. I. Kim, *Phys. Rev. B* **90**, 195136 (2014)

(35) K. Kim, S. Kim, K.-T. Ko, H. Lee, J.-H. Park, J. J. Yang, S.-W. Cheong and B. I. Min, *Phys. Rev. Lett.* **114**, 136401 (2015)

(36) S. Idelta, D. Zhang, A. G. Dijkstra, S. Artyukhin, S. Keskin, R. Cingolani, T. Shimojima, Kyoko Ishizaka, H. Ishii, K. Kudo, M. Nohara and R. J. D. Miller, *Sci. Adv.* **4**, eaar3867 (2018)

(37) C. Monney, A. Schuler, T. Jaouen, M.-I. Mottas, Th. Worlf, M. Merz, M. Muntwiler, L. Castiglioni, P. Aebi, F. Weber and M. Hengsberger, *Phys. Rev. B* **97**, 075110 (2018)

(38) D. Mazumdar, K. Haule, J. J. Yang, G. L. Pascut, B. S. Holinsworth, K. R. O'Neal, V. Kiryukhin, S.-W. Cheong and L. Musfeldt, *Phys. Rev. B* **91**, 041105(R) (2015)

(39) B. Joseph, M. Bendele, L .Simonelli, L. Maugeri, S. Pyon, K. Kudo, M. Nohara, T. Mizokawa and N. L. Saini, *Phys. Rev. B* **88**, 224109 (2013).

(40) T. Mizokawa, *J. Phys.: Conference Series* **428**, 012020 (2013)

(41) B. J. Kim, H. Jin, S. J. Moon, J.-Y. Kim, B.-G. Park, C. S. Leem, J. Yu, T. W. Noh, C. Kim, S.-J. Oh, J.-H. Park, V. Duriraj, G. Cao and E. Rotenberg, *Phys. Rev. Lett.* **101**, 076402 (2008)

(42) B. J. Kim, H. Ohsumi, T. Komesu, S. Sakai, T. Morita, H. Takagi and T. Arima, *Science* **323**, 1329-1332 (2009)

(43) S. Fujiyama, H. Ohsumi, T. Komesu, J. Matsuno, B. J. Kim, M. Takata, T. Arima and H. Takagi, *Phys. Rev. Lett.* **108**, 247212 (2012)

(44) P.-J. Hsu, T. Mauerer, M. Vogt, J. J. Yang, Y. S. Oh, S.-W. Cheong, M. Bode and W. Wu, *Phys. Rev. Lett.* **111**, 266401 (2013)

(45) W. Ruan, P. Tang, A. Fang, P. Cai, C. Ye, X. Li, W. Duan, N. Wang and Y. Wang, *Sci. Bull.* **60**, 798-805 (2015)

(46) Q. Li, W. Lin, J. Yan, X. Chen, A. G. Gianfrancesco, D. J. Singh, D. Mandrus, S. V. Kalinin and M. Pan, *Nat. Commun.* **5**, 5358 (2014)

(47) T. Mauerer, M. Vogt, P.-J. Hsu, G. L. Pascut, K. Haule, V. Kiryukhin, J. Yang, S.-W. Cheong, W. Wu and M. Bode, *Phys. Rev. B* **94**, 014106 (2016)

(48) T. Machida, Y. Fujisawa, K. Igarashi, A. Kaneko, S. Ooi, T. Mochiku, M. Tachiki, K. Komori, K. Hirata and H. Sakata, *Phys. Rev. B* **88**, 245125 (2013)

(49) J. Dai, K. Haule, J. J. Yang, Y. S. Oh, S.-W. Cheong and W. Wu, *Phys. Rev. B* **90**, 235121 (2014)

(50) H. S. Kim, T.-H. Kim, J. Yang, S.-W. Cheong and H. W. Yeom, *Phys. Rev. B* **90**, 201103(R) (2014)

(51) C. Chen, J. Kim, Y. Yang, G. Cao, R. Jin and E. W. Plummer, *Phys. Rev. B* **95**, 094118 (2017)

(52) K. Mizuno, K. Magishi, Y. Shinonome, T. Saito, K. Koyama, N. Matsumoto, S. Nagata, *Physica B* **312-313**, 818-819 (2002)

(53) A. F. Fang, G. Xu, T. Dong, P. Zheng and N. L. Wang, *Sci. Rep.* **3**, 1153 (2013)

(54) M. Kamitani, S. Bahramy, R. Arita, S. Seki, T. Arima, Y. Tokura and S. Ishiwata, *Phys. Rev. B* **87**, 180501 (R) (2013)

(55) K. Kudo, M. Kobayashi, S. Pyon and M. Nohara, *J. Phys. Soc. Jpn.* **82**, 085001 (2013)

(56) H. Lei, K. Wang, M. Abeykoon, E. Bozin, J. B. Warren and C. Petrovic, *arXiv*:1307.7029 (2013)

(57) S. Pyon, K. Kudo and M. Nohara, *J. Phys. Soc. Jpn.* **81**, 053701 (2012)

(58) A. Kiswandhi, J. S. Brooks, H. B. Cao, J. Q. Yan, D. Mandrus, Z. Jiang and H. D. Zhou, *Phys. Rev. B* **87**, 121107(R) (2013)

(59) S. Pyon, K. Kudo and M. Nohara, *Physica C* **494**, 80-84 (2013)

(60) S. Y. Zhou, X. L. Li, B. Y. Pan, X. Qiu, J. Pan, X. C. Hong, Z. Zhang, A. F. Fang, N. L. Wang and S. Y. Li, *EPL* **104**, 27010 (2013)

(61) D. J. Yu, F. Yang, L. Miao, C. Q. Han, M.-Y. Yao, F. Zhu, Y. R. Song, K. F. Zhang, J. F. Ge, X. Yao, Z. Q. Zou, Z. J. Li, B. F. Gao, C. Liu, D. D. Guan, C. L. Gao, D. Qian and J.-F. Jia, *Phys. Rev. B* **89**, 100501(R) (2014)

(62) Y. Fujisawa, T. Machida, K. Igarashi, A. Kaneko, T. Mochiku, S. Ooi, M. Tachiki, K. Komori, K. Hirata and H. Sakata, *J. Phys. Soc. Jpn.* **84**, 043706 (2015)

(63) Y. Fujisawa, T. Machida, K. Igarashi, A. Kaneko, T. Mochiku, S. Ooi, M. Tachiki, K. Komori, K. Hirata and H. Sakata, *Physica C: Superconductivity and its applications* **530**, 35-37 (2016)

(64) M. Kamitani, H. Sakai, Y. Tokura and S. Ishiwata, *Phys. Rev. B* **94**, 134507 (2016)

(65) O. Ivashko, L. Yang, D. Destraz, E. Martino, Y. Chen, C. Y. Guo, H. Q. Yuan, A. Pisoni, P. Matus, S. Pyon, K. Kudo, M. Nohara, L. Forró, H. M. Ronnow, H. Hücker, M. V. Zimmermann and J. Chang, *Sci. Rep.* **7**, 17157 (2017)

(66) T. Mochiku, Y. Matsushita, A. Sato, Y. Fujisawa, K. Igarashi, T. Machida, H. Sakata and K. Hirata, *Phys. Procedia* **58**, 90-93 (2014)

(67) J.-Q. Yan, B. Saparov, A. S. Sefat, H. Yang, H. B. Cao, H. D. Zhou, B. C. Sales and D. G. Mandrus, *Phys. Rev. B* **88**, 134502 (2013)

(68) R. Yu, S. Banerjee, H. C. Lei, R. Sinclair, M. Abeykoon, H. D. Zhou, C. Petrovic, Z. Guguchia and E. S. Bozin, *Phys. Rev. B* **97**, 174515 (2018)

(69) A. Glamazda, K.-Y. Choi, P. Lemmens, J. J. Yang and S.-W. Cheong, *New J. Phys.* **16**, 093061 (2014)

(70) X. Li, J.-Q. Yan, D. J. Singh, J. B. Goodenough and J.-S. Zhou, *Phys. Rev. B* **92**, 155118 (2015)

(71) E. Paris, B. Joseph, A. Iadecola, C. Marini, H. Ishii, K. Kudo, S. Pascarelli, M. Nohara, T. Mizokawa and N. L. Saini, *Phys. Rev. B* **93**, 134109 (2016)

(72) S. Park, S. Y. Kim. H. K. Kim, M. J. Kim, T. Kim, H. Kim, G. S. Choi, C. J. Won, S. Kim, K. Kim, E. F. Talantsev, K. Watanabe, T. Taniguchi, S.-W. Cheong, B. J. Kim, H. Wh. Yeom, J. Kim, T.-H. Kim and J. S. Kim, *Nat. Commun.* **12**, 3157 (2021)

(73) M. Yoshida, K. Kudo, M. Nohara and Y. Iwasa, *Nano Lett.* **18**, 3113-3117 (2018)

(74) M. Clandra, I. I. Mazin and F. Mauri, *Phys. Rev. B* **80**, 241108(R) (2009)

(75) M. Yoshida, Y. Zhang, J. Ye, R. Suzuki, Y. Imai, S. Kimura, A. Fujiwara and Y.

Iwasa, *Sci. Rep.* **4**, 7302 (2014)

(76) M. Yoshida, J. Ye, Y. Zhang, Y. Imai, S. Kimura, A. Fujiwara, T. Nishizaki, N. Kobayashi, M. Nakano and Y. Iwasa, *Nano Lett.* **17**, 5567-5571 (2017)

(77) H. S. Kim, S. Kim, K. Kim, B. I. Min, Y.-H. Cho, L. Wang, S.-W. Cheong and H. W. Yeom, *Nano Lett.* **16**, 4260-4265 (2016)

(78) H. Oike, M. Kamitani, Y. Tokura and F. Kagawa, *Sci. Adv.* **4**, eaau3489 (2018)

(79) J. Hwang, K. Kim, C. Zhang, T. Zhu, C. Herbig, S. Kim, B. Kim, Y. Zhong, M. Salah, M. M. El-Desoky, C. Hwang, Z.-X. Shen, M. F. Crommie and S.-K. Mo, *Nat. Commun.* **13**, 906 (2022)

(80) J. Hwang, Y. Jin, C. Zhang, T. Zhu, K. Kyoo, Y. Zhong, J.-E. Lee, Z. Shen, Y. Chen, W. Ruan, H. Ryu, C. Hwang, J. Lee, M. F. Crommie, S.-K. Mo and Z.-X. Shen, *Adv. Mater.* **34**, 2204579 (2022)

(81) Y. Song, C. Jia, H. Xiong, B. Wang, Z. Jiang, K. Huang, J. Hwang, Z. Li, C. Hwang, Z. Liu, D. Shen, J. A. Sobota, P. .Kirchmann, J. Xue, T. P. Devereaux, S.-K. Mo, Z.-X. Shen and S. Tang, *Nat. Commun.* **14**, 1116 (2023)

(82) Y. Chen, W.-Y. He, W. Ruan, J. Hwang, S. Tang, R. L. Lee, M. Wu, T. Zhu, C. Zhang, H. Ryu, F. Wang, S. G. Louie, Z.-X. Shen, S.-K. Mo, P. A. Lee and M. F. Crommie, *Nat. Phys.* **18**, 1335-1340 (2022)

(83) W. Ruan, Y. Chen, S. Tang, J. Hwang, H.-Z. Tsai, R. L. Lee, M. Wu, H. Ryu, S. Kahn, F. Liou, C. Jia, A. Aikawa, C. Hwang, F. Wang, Y. Choi, S. G. Louie, P. A. Lee, Z.-X. Shen, S.-K. Mo and M. F. Crommie, *Nat. Phys.* **17**, 1154-1161 (2021)

(84) S. Tang, C. Zhang, D. Wong, Z. Pedramrazi, H.-Z. Tsai, C. Jia, B. Moritz, M. Claassen, H. Ryu, S. Kahn, J. Jiang, H. Yan, M. Hashimoto, D. Lu, R. G. Moore, C.-C. Hwang, C. Hwang, Z. Hussain, Y. Chen, M. M. Ugeda, Z. Liu, X. Xie, T. P. Devereaux, M. F. Crommie, S.-K. Mo and Z.-X. Shen, *Nat. Phys.* **13**, 683-687 (2017)

(85) Y. Zhang, T.-R. Chang, B. Zhou, Y.-T. Cui, H. Yan, Z. Liu, F. Schmitt, J. Lee, R. Moore, Y. Chen, H. Lin, H.-T. Jeng, S.-K. Mo, Z. Hussain, A. Bansil and Z.-X. Shen, *Nat. Nanotech.* **9**, 111-115 (2014)

(86) S. V. Streltsov and D. I. Khomskii, *Phys. Uspekhi* **60**, 1121 (2017)

(87) E. S. Bozin, A. S. Masadeh, Y. S. Hor, J. F. Mitchell and S. J. L. Billinge, *Phys. Rev. Lett.* **106**, 045501 (2011)

(88) E. S. Bozin, W. G. Yin, R. J. Koch, M. Abeykoon, Y. S. Hor, H. Zheng, H. C. Lei, C. Petrovic, J. F. Mitchell and S. J. L. .Billinge, *Nat. Commun.* **10**, 3638 (2019)

(89) C.-Y. Lim, S. Kim, S. W. Jung, J. Hwang and Y. Kim, *Curr. Appl. Phys.* **60**, 43-56 (2024)

(90) A. Wang, Z. Liu, J. Pan, Q. Li, G. Li, Q. Huan, S. Du and H.-J. Gao, *Chin. Phys. B* **29**, 078102 (2020)

(91) H. K. Kim, S. Y. Kim, C. J. Won, S.-W. Cheong, J. Kim, J. S. Kim and T.-H. Kim, *Phys. Rev. B* **107**, 045112 (2023)

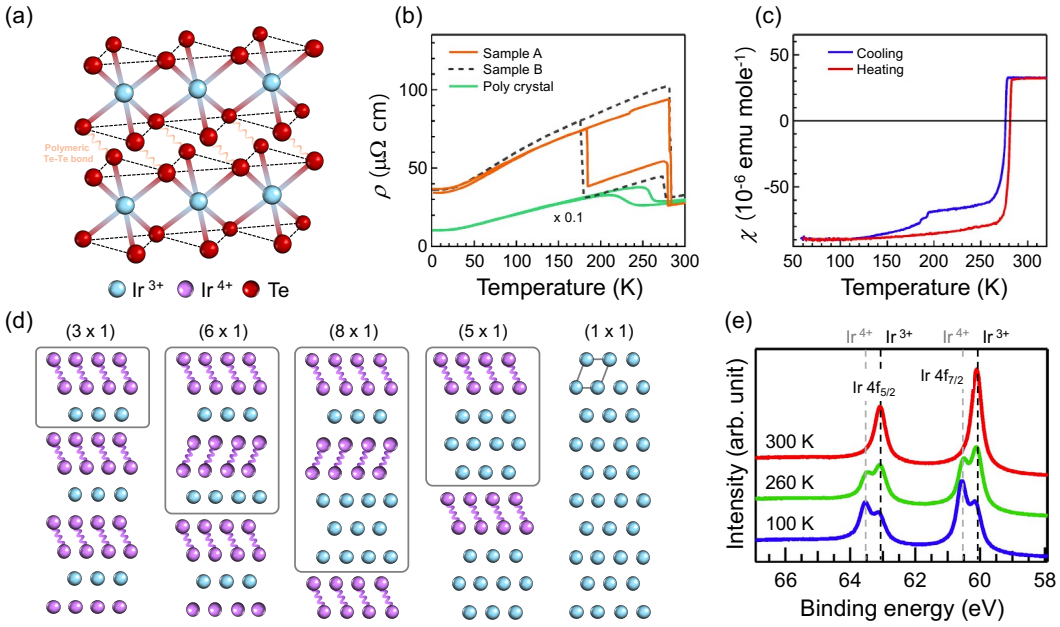

Figure 1: (Color online) **Crystal structure and physical properties of 1*T*-IrTe$_2$.** (a) Schematics of the crystal structure of bulk 1*T*-IrTe$_2$. The orange wavy lines represent the polymeric Te-Te bond. (b,c) Temperature dependent electrical resistivity and magnetic susceptibility for bulk 1*T*-IrTe$_2$, respectively. (d) Schematics of possible formations of stripe charge orderings in IrTe$_2$. The boxes indicate the unit cell of the charge ordered phases. (e) Ir 4*f* core level photoemission spectra for bulk IrTe$_2$ taken at 300 K (HT), 260 K ($\mathbf{q}_{1/5}$) and 100 K ($\mathbf{q}_{1/5}$). Vertical left and right dashed lines represent the peak positions of Ir^{4+} and Ir^{3+}, respectively. Figs .1 (b,c,e) are adapted from Ref. [15] © 2015 Springer Nature. Figs. 1 (a,d) are created by the authors.

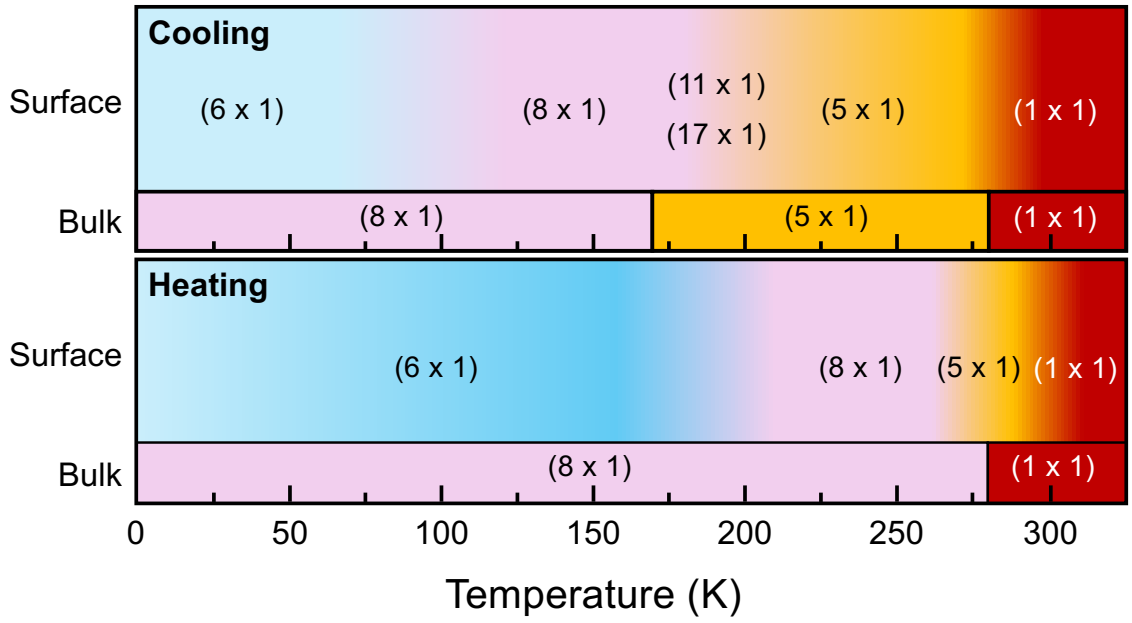

Figure 2: (Color online) Summary of surface and bulk charge orderings in 1*T*-$IrTe_2$ depending on temperatures for (upper panel) cooling and (lower panel) heating processes. The figure is created by the authors taking Ref. [15,18,44,51] as references.

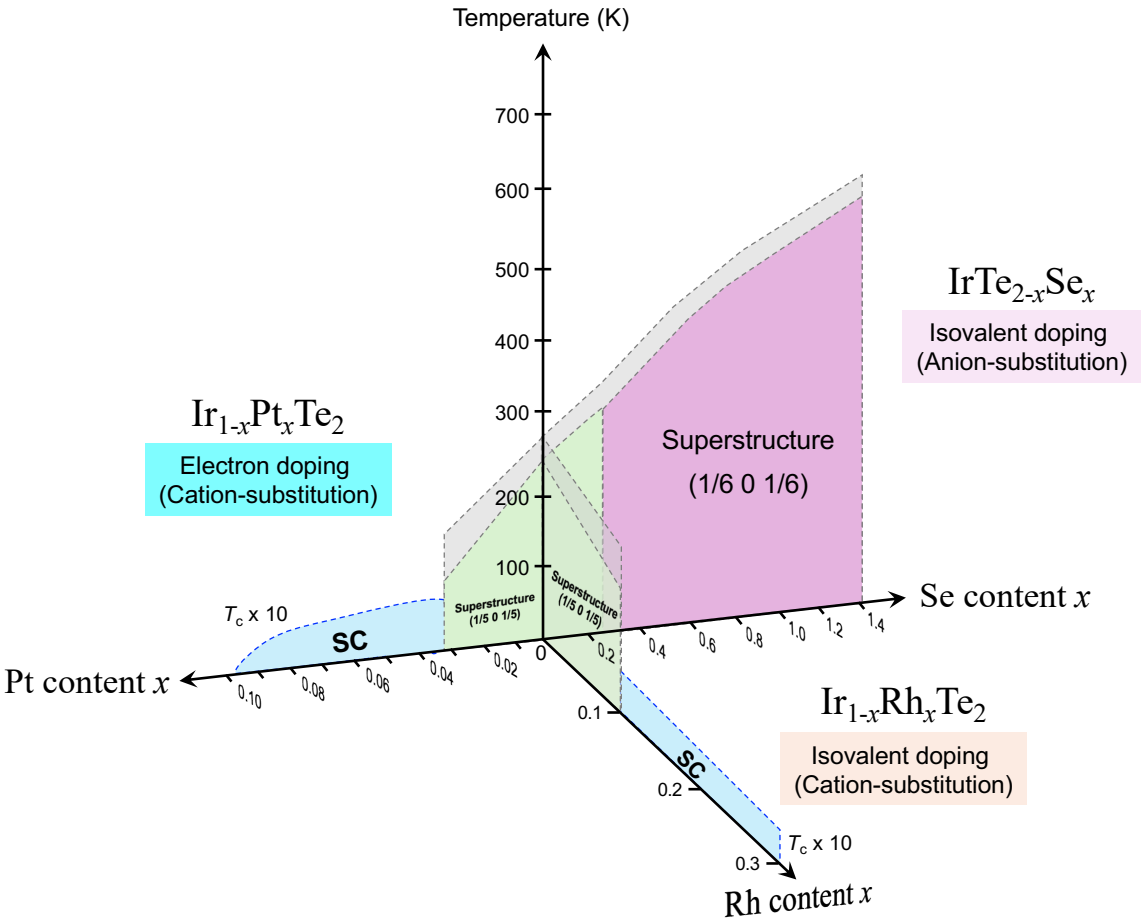

Figure 3: (Color online) **Schematics for the phase diagrams of cation- and anion-substituted 1*T*-$IrTe_2$.** Cation-substitutions of Ir with Pt and Rh serve as electron- and isovalent dopings for 1*T*-$IrTe_2$ in the phase diagram, respectively. Anion-substitution of Te with Se also provides an isovalent doping. The figure is created by the authors taking Ref. [18,29,55,57] as references.

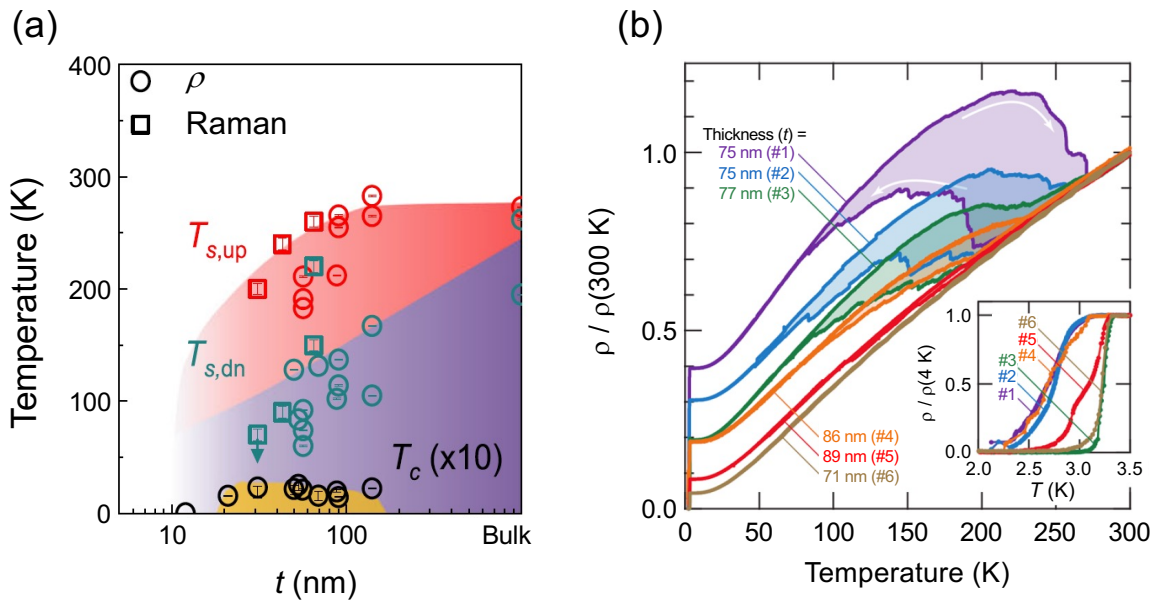

Figure 4: (Color online) **Thickness-dependent phase diagram of 1*T*-IrTe$_2$ nanoflakes**. (a) Phase diagram of IrTe$_2$ nanoflakes as a function of thickness t. $T_{s,up}$ and $T_{s,dn}$ represent transition temperatures for warming (up) and cooling (down) processes, respectively. Top and bottom backgrounds indicate the charge-ordered states in the phase diagram for warming and cooling processes, respectively. A lower bottom area is the superconducting state. (b) Temperature-dependence of normalized resistivity [$\rho(T)$ / ρ(300 K)] for the IrTe$_2$ nanoflakes. Figures are reproduced from Refs. [72] © 2021 Springer Nature and [73] © 2018 American Chemical Society.

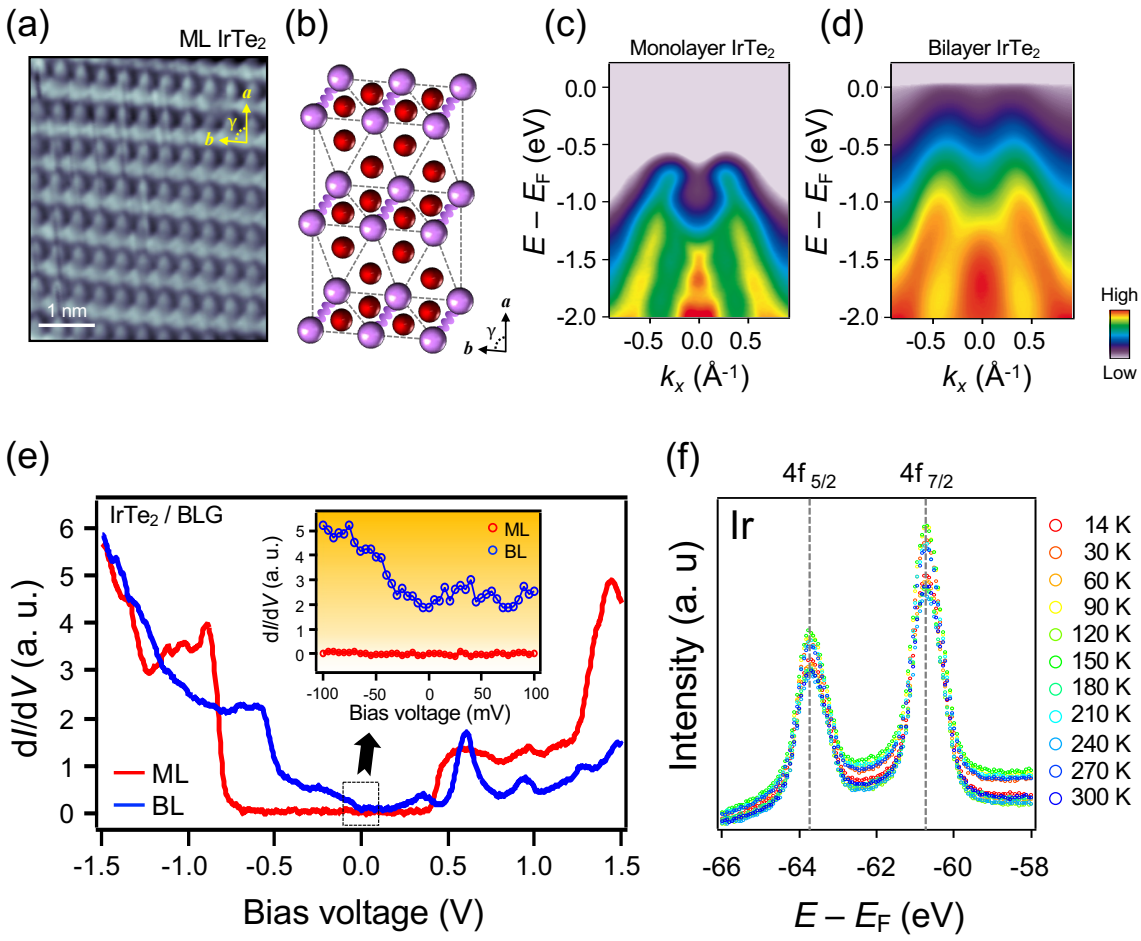

Figure 5: (Color online) **Crystal structure and electronic properties of ML and BL 1*T*-IrTe$_2$**. (a,b) Atomically-resolved STM image and a schematics of a top view of 2 × 1 dimer structure of ML IrTe$_2$, respectively. (b,c) ARPES band structures of (c) ML and (d) BL 1*T*-IrTe$_2$. (e) The STS d*I*/d*V* spectra for ML and BL IrTe$_2$. The inset is a close-up look of the dashed box near Fermi energy. (f) Temperature-dependent Ir 4*f* core level spectra. Figures are reproduced from Ref. [79] © 2022 Springer Nature.